

1 Running title: Loss of synchronized intra-islet Ca²⁺ oscillations *in vivo* in *Robo*-deficient β cells

2

3 **Islet architecture controls synchronous β cell response to glucose in the intact mouse**
4 **pancreas *in vivo***

5

6 Melissa T. Adams¹, Christopher A. Reissaus², Joseph M. Szulczewski¹, JaeAnn M. Dwulet³,

7 Melissa R. Lyman¹, Sophia M. Sdao⁴, Sutichot D. Nimkulrat¹, Suzanne M. Ponik¹, Matthew J.

8 Merrins⁴, Richard K.P. Benninger³, Raghavendra G. Mirmira⁵, Amelia K. Linnemann², Barak

9 Blum^{1*}

10

11 ¹Department of Cell and Regenerative Biology, University of Wisconsin-Madison, Madison, WI
12 53705, USA

13 ²Herman B Wells Center for Pediatric Research and Center for Diabetes and Metabolic Diseases,
14 Indiana University School of Medicine, Indianapolis, IN 46202, USA

15 ³Department of Bioengineering and Barbara Davis Center for Diabetes, University of Colorado
16 Denver, Anschutz Medical Campus, Aurora, CO. 80045, USA

17 ⁴Department of Medicine, Division of Endocrinology, Diabetes, and Metabolism, University of
18 Wisconsin-Madison, Madison, Wisconsin 53705, USA

19 ⁵Kovler Diabetes Center and the Department of Medicine, University of Chicago, Chicago, IL
20 60637, USA

21

22 ***Lead contact and Corresponding Author:** Barak Blum; bblum4@wisc.edu

23 **Abstract**

24 The spatial architecture of the islets of Langerhans is hypothesized to facilitate synchronized
25 insulin secretion between β cells, yet testing this *in vivo* in the intact pancreas is challenging.
26 *Robo* β KO mice, in which the genes *Robo1* and *Robo2* are deleted selectively in β cells, provide
27 a unique model of altered islet architecture without loss of β cell differentiation or islet damage
28 from diabetes. Combining *Robo* β KO mice with intravital microscopy, we show here that *Robo*
29 β KO islets lose synchronized intra-islet Ca^{2+} oscillations between β cells *in vivo*. We provide
30 evidence that this loss is not due to a β cell-intrinsic function of Robo, loss of Connexin36 gap
31 junctions, or changes in islet vascularization, suggesting that the islet architecture itself is
32 required for synchronized Ca^{2+} oscillations. These results will have implications for
33 understanding structure-function relationships in the islets during progression to diabetes as
34 well as engineering islets from stem cells.

35 Introduction

36 The islets of Langerhans, which comprise the endocrine pancreas, are highly organized
37 micro-organs responsible for maintaining blood glucose homeostasis. Islets are composed of
38 five endocrine cell types (α , β , δ , PP, and ϵ) which, in rodents, are arranged such that the β cells
39 reside in the core of the islet, while other non- β endocrine cells populate the islet mantle¹.
40 Human islet architecture is more complex; however, it still follows non-random patterning in
41 which multiple core-mantle-like units comprise a single islet². In both rodent and human islets,
42 respective stereotypical islet architectures prioritize homotypic over heterotypic interactions
43 between endocrine cell types³. The biological reason for preferential homotypic interactions
44 between endocrine cells is not completely clear, but it has been suggested to be important for
45 dictating the level of Connexin36 (Cx36)-mediated electrical β cell- β cell coupling, thus
46 controlling synchronization of glucose-stimulated insulin secretion (GSIS) between neighboring
47 β cells^{4,5}.

48 Synchronous insulin secretion between β cells is triggered when glucose from the blood
49 enters the β cells through glucose transporters. As this glucose is metabolized, the ratio of
50 intracellular ATP/ADP in the cells increases. The rise in ATP causes ATP sensitive K^+ channels to
51 close, resulting in membrane depolarization. The resultant depolarization causes voltage-gated
52 Ca^{2+} channels to open, triggering an influx of Ca^{2+} into the cell, which in turn promotes
53 exocytosis of insulin granules⁶⁻⁸. This chain of events is cyclical and thus results in oscillations of
54 membrane potential, cytosolic Ca^{2+} levels, and insulin secretion in response to glucose⁹.
55 Because β cells within an islet are gap-junctionally coupled, and thus electrically coupled, these
56 oscillations are synchronous across all islet β cells¹⁰. It is thus hypothesized that preferential β

57 cell homotypic contact allows for the necessary amount of gap junctions to form between
58 neighboring β cells in order to synchronize the oscillations in an entire islet, facilitating pulsatile
59 insulin secretion^{5,11}. Indeed, modeling experiments in which the number of homotypic β cell- β
60 cell nearest neighbor connections is lowered within an islet result in predicted perturbation of
61 synchronous Ca^{2+} oscillations⁵. If this *in silico* prediction is correct, then disrupting spatial
62 organization of the different endocrine cell types within the islet alone, without affecting any
63 other property of the cells, should be sufficient to disturb synchronized insulin secretion
64 between β cells. However, direct empirical evidence for this hypothesis is lacking.

65 Most genetic mouse models that show disruption of islet architecture also display
66 defects in glucose homeostasis¹². However, in many of these models, the disrupted islet
67 architecture phenotype is linked to either developmental defects in β cell differentiation or
68 maturation¹³⁻²⁴ or to pathologies related to β cell damage in diabetes²⁵⁻³⁰. This introduces a
69 strong confounding factor for studying the role of islet architecture on β cell function.
70 Therefore current mouse models of disrupted islet architecture unsuitable for directly testing
71 the hypothesis that the preferential homotypic β cell- β cell interactions, dictated by canonical
72 islet architecture, regulate synchronized insulin secretion between β cells within the same islet.

73 Recently, we have described a mouse model in which the cell-surface receptors *Robo1*
74 and *Robo2* are deleted specifically in β cells (*Robo* β KO), resulting in disruption of canonical
75 endocrine cell type sorting within the islets³¹. Unlike other models of disrupted islet
76 architecture, the β cells in the islets of *Robo* β KO express normal levels of markers for β cell
77 differentiation and functional maturity, and do not display markers of β cell damage or stress.

78 We reasoned that this model would allow us to directly test the role of islet architecture on
79 synchronous islet oscillations between β cells in a fully differentiated, non-diabetic islet setting.

80

81 **Results**

82 ***Robo* β KO islets express mature β cell markers despite having disrupted islet architecture and 83 endocrine cell type intermixing**

84 We have previously shown that genetic deletion of *Robo1* and *Robo2* selectively in β
85 cells using either *Ins1-Cre; Robo1* ^{Δ/Δ} *2*^{*flx/flx*} or *Ucn3-Cre; Robo1* ^{Δ/Δ} *2*^{*flx/flx*} mice (*Robo* β KO) results in
86 disrupted islet architecture and endocrine cell type sorting without affecting β cell death,
87 proliferation, or the expression of the β cell maturation markers MafA and Ucn3³¹. To verify
88 that β cells in *Robo* β KO islet are truly mature, we expanded the analysis to look at transcript
89 levels of all maturity markers. We performed RNA sequencing and differential gene expression
90 analysis on FACS-purified β cells from both *Robo* β KO and control islets, and observed no
91 change in transcript levels of any hallmark β cell maturity or differentiation genes ($n=2$ mice of
92 each genotype; **Supplemental Figure 1**). Thus, unlike other mouse models with disrupted islet
93 architecture, β cells in *Robo* β KO islets maintain maturity and differentiation despite loss of
94 normal islet architecture.

95

96 ***Robo* β KO islets have fewer homotypic β cell- β cell contacts than control islets**

97 *In silico* simulations where the degree of β cell- β cell coupling is changed through a
98 decrease in homotypic nearest neighbors predict that disruption in islet architecture will disrupt
99 synchronous intra-islet Ca²⁺ oscillations and hormone secretion pulses^{3,5,32}. To test whether β

100 cells in *Robo* βKO islets have fewer homotypic β cell neighbors on average than control islets,
101 we performed nearest neighbor analysis on islets from pancreatic sections from *Robo* βKO and
102 control mice (**Figure 1**). We found that *Robo* βKO islets possess significantly fewer β cell- β cell
103 contacts ($n=9-11$ islets for 3 mice from each genotype; control 75.35%, *Robo* βKO 50.37%,
104 $p=0.01$), and homotypic contacts in general when compared to control islets ($n=9-11$ islets for 3
105 mice from each genotype; control 83.7%, *Robo* βKO 64.43%, $p=0.0008$). We also found that
106 *Robo* βKO islets possess significantly more β cell- α cell contacts ($n=9-11$ islets for 3 mice from
107 each genotype; control 11.21%, *Robo* βKO 25.99%, $p=0.02$), and heterotypic contacts in general
108 when compared to control islets ($n=9-11$ islets for 3 mice from each genotype; control 16.3%,
109 *Robo* βKO 35.57%, $p=0.0008$). Together, this suggests that *Robo* βKO islets make fewer
110 homotypic β cell- β cell connections compared to control islets. We reasoned that the altered
111 degree of homotypic β cell- β cell interaction in *Robo* βKO islets together with the seemingly
112 retained β cell maturity provide a unique model by which to test the hypothesis that endocrine
113 cell type organization affects synchronous insulin secretion in the islet.

114

115 ***Robo* βKO islets display unsynchronized Ca^{2+} oscillations *in vivo***

116 To investigate how the reduced homotypic β cell- β cell connections in *Robo* βKO islets
117 affects insulin-secretion dynamics, we adopted a novel intravital Ca^{2+} imaging method which
118 enables imaging of islet Ca^{2+} dynamics *in situ* within the intact pancreas³³. In brief, this method
119 employs an intravital microscopy (IVM) platform and adeno-associated viral (AAV) delivery of
120 insulin promoter-driven GCaMP6s, a fluorescent Ca^{2+} biosensor, to quantitate β cell Ca^{2+}
121 dynamics *in vivo* in both *Robo* βKO and control islets. This method thus allows for retention of

122 the islet's *in vivo* microenvironment, blood flow, and innervation, and provides more realistic
123 conditions than *in vitro* approaches allow for.

124 We verified that synchronous Ca^{2+} oscillations are maintained *in vivo* in islets by
125 measuring GCaMP6s intensity of β cells within AAV8-RIP-GCaMP6 infected islets of control
126 (*Robo WT*) mice (**Figure 2**). As expected, control mice displayed whole islet synchronous Ca^{2+}
127 oscillations for at least 10 minutes after glucose elevation ($n=3$ islets from 1 mouse; **Figure 2**
128 and **Supplemental Video 1**). We quantified the degree to which these oscillations are
129 synchronous within the islet by analyzing the amount of correlation between GCaMP6s active
130 areas within individual islets. While oscillations vary in frequency between islets, the degree of
131 correlation between β cells within any one islet is very high, confirming that control islets
132 possess highly synchronous intra-islet Ca^{2+} oscillation *in vivo* (fraction of GCaMP6s activity with
133 correlated Ca^{2+} oscillations= 0.97 ± 0.005 , $n=3$ islets from 1 mouse; see Figure 4A).

134 Conversely, we found that most *Robo β KO* islets display asynchronous intra-islet Ca^{2+}
135 oscillations *in vivo* (**Figure 3, Supplemental Figure 2, Supplemental Videos 2 and 3**).
136 Quantification of this asynchronous behavior through correlation analysis of GCaMP6s activity
137 within individual *Robo β KO* islets revealed significant reduction in intra-islet correlated
138 oscillation areas compared to controls (fraction of GCaMP6s activity with correlated Ca^{2+}
139 oscillations= 0.62 ± 0.1 , $n=8$ islets from 4 mice, $p<0.01$; **Figure 4A**). Further, asynchronous *Robo*
140 *β KO* islets showed spatially distinct areas within the islet that oscillated synchronously with
141 immediate β cell neighbors but not with more distant regions within the same islet (**Figure 3C-**
142 **D, and Supplemental Figure 2**). This was not due to differences in the proportion of GCaMP6s
143 positive cells showing elevated Ca^{2+} activity within *Robo β KO* islets compared to controls

144 (control islets 0.98 ± 0.008 fraction active, $n=3$ islets from 1 mouse; *Robo* βKO islets 0.96 ± 0.02
145 fraction active, $n=5$ islets from 3 mice, $p=0.35$; **Figure 4B**).

146 Interestingly, 3 out of the 8 *Robo* βKO islets imaged showed synchronous Ca^{2+} activity in
147 greater than 90% of GCaMP6s positive areas (**Figure 4A, Supplemental Figure 3 and**
148 **Supplemental video 4**). Moreover, upon performing organ clearing and imaging on *Robo* βKO
149 pancreata, we observed multiple islets with relatively few α cells penetrating the β cell core
150 (**Figure 5, Supplemental Videos 5 and 6**). It is likely that those *Robo* βKO islets with normal
151 architecture are the same islets which retain synchronous Ca^{2+} oscillations. Together, these
152 observations suggest that some mechanisms governing synchronous Ca^{2+} oscillations within an
153 islet are not controlled intrinsically by *Robo* expression within β cells. This fits with the
154 hypothesis that architecture of the islet itself facilitates synchronous oscillations.

155 Further, analysis of the speed of wave propagation and time lag in the highly correlated
156 *Robo* βKO islets showed a trend towards a reduction in wave propagation speed (**Figure 4C**) and
157 an increase in time lag (**Figure 4D**) when compared to controls, though these failed to reach the
158 threshold for statistical significance (control islets wave propagation: $119.5 \pm 49.13 \mu m/sec$, $n=3$
159 islets from 1 mouse; *Robo* βKO islets wave propagation: $38.67 \pm 16.6 \mu m/sec$, $n=3$, $p=0.1940$;
160 control islets phase lag: $0.057 sec \pm 0.005$, $n=3$ islets from 1 mouse; *Robo* βKO islets phase lag:
161 $0.083 \pm 0.01 sec$, $n=3$, $p=0.0934$; **Figure 4C-F**). Islets with sub-optimal coupling have been shown
162 to display full synchronization in Ca^{2+} oscillations, but with lower wave velocity¹⁰. Because there
163 is a trend toward slower wave velocity, these *Robo* βKO islets may still have sub-optimal
164 coupling due to architecture changes despite their fully synchronized Ca^{2+} oscillations.

165

166 ***Robo* β KO islets retain the ability to form gap junctions and have similar levels of**
167 **vascularization**

168 Besides a decrease in β cell- β cell homotypic contacts within the islet, a possible
169 explanation for the loss of synchronized whole islet Ca^{2+} oscillations in *Robo* β KO islets is that β
170 cells in *Robo* β KO islets no longer possess the gap junctions necessary for adequate electrical
171 coupling. Indeed, the phenotype described above is reminiscent of that observed in mice
172 heterozygous for a *Cx36* null allele^{10,34}. To test whether *Robo* β KO mice form fewer gap
173 junctions between β cells, we measured the area of Cx36 protein immunofluorescence
174 normalized to islet area in *Robo* β KO and control islets (**Figure 6**). We observed no difference in
175 Cx36 immunofluorescence between *Robo* β KO islets and controls (**Figure 6B**), suggesting that
176 loss of synchronous intra-islet Ca^{2+} oscillations is not due to failure of gap junction formation in
177 β cells (control islets: 0.01 ± 0.002 Cx36 signal/ μm^2 , *Robo* β KO islets: 0.01 ± 0.001 Cx36
178 signal/ μm^2 , $n=10-15$, $p=0.17$ islets from 4 mice of each group).

179 Another possible explanation for the observed uncoupling of intra-islet Ca^{2+} oscillations
180 in *Robo* β KO islets is that β cell- β cell contact in *Robo* β KO is disrupted due to physical blocking
181 by non-endocrine tissue. To determine if other non-endocrine architectural changes within the
182 islet occur in *Robo* β KO mice we quantified the amount of matrix components secreted by
183 vessels as a surrogate for vasculature (laminin, and collagen IV) in *Robo* β KO and control islets.
184 In all cases we found no significant difference in area of vessel matrix components (**Figure 7**)
185 between *Robo* β KO and control islets, suggesting that interfering blood vessels are likely not the
186 cause of loss of whole islet synchronous Ca^{2+} oscillations (normalized laminin β 1 area: control
187 0.3126 ± 0.05 μm^2 , $n=10-12$ islets from 8 mice; *Robo* β KO 0.3747 ± 0.05 μm^2 , $n=10-12$ islets from 8

188 mice; $p = 0.3908$; normalized Col IV area: control $0.1812 \pm 0.01 \mu\text{m}^2$, $n = 10-12$ islets from 4 mice;
189 *Robo* βKO 0.156 ± 0.019 , $p = 0.35$).

190

191 Discussion

192 In this study, we provide evidence for the importance of islet architecture for proper
193 islet function *in vivo*. When islet architecture is disrupted while β cell maturity is retained in
194 *Robo* βKO mice, synchronized Ca^{2+} oscillations are perturbed in the *in vivo* islet. This is not due
195 to loss of Cx36, or change in amount of islet vascularization. *Robo* βKO β cells possess fewer
196 homotypic nearest neighbors than controls, suggesting a limited capacity to electrically couple
197 β cells across the islet. Taken together, these data indicate that islet architecture itself,
198 uncoupled from β cell maturity or availability of gap junction machinery is important for
199 coordinated insulin secretion between β cells.

200 *Robo*, and its ligand Slit, have been previously shown to affect Ca^{2+} oscillations in β cell
201 *in vitro*³⁵. However, while it is possible that intrinsic β cell factors rather than the disrupted islet
202 architecture alone contribute to disruption of synchronized Ca^{2+} oscillations in *Robo* βKO islets
203 in our experiments, this is not likely the driving force. If this was the case, then we would expect
204 a highly penetrant asynchronous oscillation phenotype in *Robo* βKO islets, yet more than one-
205 third of *Robo* βKO islets analyzed showed highly synchronized Ca^{2+} oscillations. Instead, these
206 results suggest that deletion of *Robo* alone in β cells is not sufficient to abolish synchronicity.
207 Moreover, *Robo* βKO islets show a heterogeneous spectrum of disrupted architecture within
208 the same animal, with some islets displaying severe endocrine cell type intermixing while
209 others retain relatively normal architecture. Thus it is likely that islets with relatively normal

210 architecture correspond to the islets that display more synchronous Ca^{2+} oscillations. Moreover
211 phenotypic heterogeneity is likely not due to an incomplete deletion of *Robo* in a subset of
212 islets. This is evident by the fact the islets were detected during the Ca^{2+} imaging experiment by
213 the fluorescent labeling of β cells with the H2B-mCherry lineage-tracing reporter³¹, which uses
214 the same Cre that is used to delete *Robo* in those β cells. Thus expression of H2B-mCherry
215 precludes inefficient Cre expression and recombination.

216 It also remains possible that other components of islet architecture besides endocrine
217 cell type sorting contribute to disruption in Ca^{2+} oscillations found in *Robo* βKO islets.
218 Specifically, while we have shown that the amount of vascularization between *Robo* βKO islets
219 and controls is similar, we cannot draw conclusions on whether the pattern of vessels is
220 unchanged. Further, it is possible that amount and patterning of innervation may vary between
221 *Robo* βKO and controls. This is particularly of interest because *Robo* has known roles in
222 angiogenesis and axon guidance, and thus could affect precisely how the islet is innervated and
223 vascularized³⁶.

224 Finally, our results may have implications towards directing islet architecture in the
225 pursuit of generating *bona fide* islets from stem cells *in vitro* for the treatment of diabetics.
226 Thus far, most efforts to create such stem cell derived islets have focused on creating
227 homogenous functionally mature β cells³⁷. Such efforts have been largely successful in terms of
228 creating β cells that display insulin secretory profiles close to those of primary β cells³⁸. Yet
229 despite their seeming resemblance to mature native β cells, islets made from stem cell-derived
230 β cells fail to fully match the function of isolated primary islets^{37,38}. This has been partially
231 attributed to the fact that stem cell derived islets formed *in vitro* thus far have been simply

232 clusters of homogenous β cells, rather than an organized heterogeneous population of β cells
233 and other islet cell types³⁷. Because of the importance of heterogeneous cell types in
234 controlling glucose homeostasis, it has become evident that achieving correct β cell
235 heterogeneity is needed to generate better islets *in vitro*³⁹. However, it is likely that addition of
236 these cells without recapitulation of islet architecture will not generate islets with optimum
237 function and β cell coupling.

238 **Acknowledgments**

239 We Kurt Weiss and Jan Huisken for help with imaging. We thank members of the Blum lab,
240 especially Jennifer Gilbert and Bayley Waters, for valuable discussion. We are also grateful to
241 Nadav Sharon and Danny Ben-Zvi for critically reading the manuscript. This work was funded in
242 part by the following grants. R01DK121706, the DRC at Washington University Pilot Grant
243 P30DK020579, and Pilot Award UL1TR000427 from the UW-Madison Institute for Clinical and
244 Translational Research (ICTR) to BB; R01DK060581 to RM; R01DK102950 and R01DK106412 to
245 RKP; R01CA216248 to SP; R01DK113103, R01AG062328, ADA 1-16-IBS-212 to MM, and an
246 award from the Wisconsin Partnership Program to BB and MM. MTA was funded by
247 5T32GM007133-44 and a graduate training award from the UW-Madison Stem Cell &
248 Regenerative Medicine Center. We also thank the University of Wisconsin Carbone Cancer
249 Center Support Grant P30CA014520 for use of the UW Flow Core, and the University of
250 Wisconsin, Madison Biotechnology Center for sequencing and analysis.

251

252 **Author Contribution**

253 Conceptualization, B.B. and M.T.A.; Methodology, B.B., M.T.A., C.A.R, and J.M.D.; Investigation,
254 M.T.A., C.A.R, J.M.S, M.R.L, S.M.S, and S.D.N; Formal Analysis, M.T.A., C.A.R, M.R.L., and J.M.D.;
255 Resources, S.M.P, R.G.M, A.K.L, M.J.M. and R.K.P.B.; Writing Original Draft, B.B and M.T.A.;
256 Writing, Review and Editing, all authors; Funding Acquisition, B.B., S.M.P, M.J.M, R.K.P.B.,
257 R.G.M., and A.K.L; Supervision, B.B.

258 **Materials and Methods**

259 **Animals**

260 The experimental protocol for animal usage was reviewed and approved by the University of
261 Wisconsin-Madison Institutional Animal Care and Use Committee (IACUC) under Protocol
262 #M005221 and Protocol #M005333, and all animal experiments were conducted in accordance
263 with the University of Wisconsin-Madison IACUC guidelines under the approved
264 protocol. *Robo1^Δ,2^{flx40}*, *Ins1-Cre⁴¹*, *Urocortin3-Cre⁴²* and *Rosa26-Lox-Stop-Lox-H2BmCherry⁴³*
265 mice were previously described. All mouse strains were maintained on a mixed genetic
266 background. Control colony mates in all analyses were *Robo^{+/+}* with the either *Ins1-Cre* or *Ucn3-*
267 *Cre*.

268

269 **Immunofluorescence**

270 Pancreata were fixed with 4% PFA at 4°C for 3h, embedded in 30% sucrose and frozen in OCT
271 (Tissue-Tek). Pancreatic sections (10 μm) were stained using a standard protocol. The following
272 primary antibodies and dilutions were used: guinea pig anti-Insulin (1:6, Dako, IR00261-2),
273 mouse anti-Glucagon (1:500, Sigma G2654), rabbit anti-Glucagon (1:200, Cell Signaling 2760S),
274 rabbit anti-Somatostatin (1:1000, Phoenix G-060-03), rabbit anti-Connexin36 (1:80, Invitrogen
275 36-4600), rabbit anti-Col IV (1:300, Abcam Ab656), rat anti-Laminin β1 (1:500, Invitrogen MA5-
276 14657). The following secondary antibodies were used at 1:500: Donkey anti-Guinea Pig 594
277 (Jackson), Donkey anti-Guinea Pig 647 (Jackson), Donkey anti-Rabbit 488 (Invitrogen), Donkey
278 anti-Rabbit 594 (Invitrogen), Donkey anti-goat 647 (Invitrogen), and Donkey anti-rat 488

279 (Invitrogen). Slides were imaged using a Leica SP8 Scanning Confocal microscope or a Zeiss Axio
280 Observer.Z1 microscope.

281

282 **RNA sequencing**

283 RNA was isolated from FACS sorted lineage-traced β cells³¹ from control and *Robo* β KO mice
284 using phenol chloroform extraction (TRIzol). DNA libraries were generated using Takara's
285 SMART-Seq v4 Low Input RNA Kit for Sequencing (Takara, Mountain View, California, USA) for
286 cDNA synthesis and the Illumina NexteraXT DNA Library Preparation (Illumina, San Diego, CA,
287 USA) kit for cDNA dual indexing. Full length cDNA fragments were generated from 1-10ng total
288 RNA by SMART (Switching Mechanism at 5' End of RNA Template) technology. cDNA fragments
289 were fragmented and dual indexed in a single step using the Nextera kit's simultaneous
290 transposon and tagmentation step. Quality and quantity of completed libraries were assessed
291 using Agilent DNA series chip assay (Agilent Technologies, Santa Clara, CA) and Invitrogen Qubit
292 ds DNA HS Kit (Invitrogen, Carlsbad, California, USA), respectively. Each library was standardized
293 to 2nM. Cluster generation was performed on Illumina cBot, with libraries multiplexed for
294 1x100bp sequencing using TruSeq 100bp SBS kit (v4) on an Illumina HiSeq2500. Images were
295 analyzed using standard Illumina Pipeline, version 1.8.2.

296

297 **Intravital Imaging**

298 Mouse pancreata were exposed in anesthetized mice by making a small incision on the right
299 side of the mouse, and externalizing the tip of the pancreas. A glass dish was placed over the
300 exposed pancreas and the mouse was placed on a microscope stage with isoflurane anesthesia

301 for the remainder of imaging. Islets were identified on the surface of the pancreas by detecting
302 Histone H2BmCherry fluorescent nuclei labeled by β cell-specific lineage-tracing reporter³¹.
303 Once islets were identified, mice were given injections of 1g/kg body weight glucose (30% in
304 saline) intraperitoneally. Blood glucose levels were monitored through tail vein bleeds. Once
305 the blood glucose reached \sim 300 mg/dL, GCaMP6s activity was identified using the microscope
306 eye piece. When imaging a time course of GCaMP6s intensity, a z-stack was set to 8 or 12 slices
307 each 8 μ m apart. Images were captured every 10 or 30 seconds respectively over 10 minutes at
308 a resolution of 512x512 pixels. After time courses were recorded, high resolution image z-stacks
309 were taken with 60 z planes taken 1 μ m apart or 8 z-planes taken 8 μ m apart at 1024x1024 pixel
310 resolution. For some images, rhodamine-dextran was injected retro-orbitally to mark the
311 vasculature of the islets *in vivo*.

312

313 **Gap junction and vasculature quantification**

314 Cx36 levels were quantified from images of islets co-stained with rabbit anti-Cx36 (Invitrogen)
315 and Guinea Pig anti-insulin antibody. Vasculature levels were quantified from images co-stained
316 with rat anti-Laminin β 1 or rabbit anti-col IV and guinea pig anti-insulin. 8 Z-planes were taken
317 1 μ m apart on a Leica SP8 Scanning Confocal microscope using a 40x oil immersion objective
318 (Cx36) or 20X (vasculature). Threshold masks were made of both channels for each islets, and
319 the area of each staining was measured using FIJI's analyze particles functions. The area of gap
320 junctions, blood vessels (marked by their respective antibody) was divided by the area of insulin
321 for each islet. 10-14 islets were analyzed for $n=2-8$ mice for each genotype. Student's T-test was
322 performed to obtain *P* values.

323

324 **Nearest Neighbor Analysis**

325 β cells were identified using the lineage tracer *Rosa26-Lox-Stop-Lox-H2BmCherry* crossed to
326 *Ucn3-Cre* and tissue sections were stained with antibodies against glucagon and somatostatin
327 to identify α and δ cells respectively. The 3D Tissue Spatial Analysis Toolbox for Fiji⁴⁴ was used
328 to identify specific cell types using the above markers and to calculate the number of cell type
329 specific nearest neighbors from all identified endocrine cells. Analysis was performed on 9-11
330 islets from $n=3$ mice from each genotype.

331

332 **Whole Organ Clearing and Imaging**

333 Pancreata were fixed in 4% PFA for 3 hours at room temperature, then dehydrated stepwise in
334 methanol (33, 66%, and 100%) for 15 mins each step. Samples were then bleached using
335 MeOH:H₂O₂:DMSO bleaching buffer in a 2:1:3 ratio at RT for 24 hr, and then stored in methanol
336 overnight. Next, Samples were freeze-thawed for at least 5 cycles of 24 hour freeze then 2 hour
337 thaw in -80°C-RT to facilitate antibody penetration. Samples were then rehydrated stepwise
338 back to TBST (33%, 66%, 100%), at least 15 min/step, reducing the MeOH during each step.
339 Samples were then blocked in TBST with 10% donkey serum, 5% DMSO and 0.01% NaAz for 12-
340 24 hr at RT. Samples were then incubated with primary antibodies (Dako guinea pig anti-Insulin
341 and CST Rabbit anti-glucagon) in blocking buffer for 48 hr- 72 hr, then washed overnight in
342 TBST. Following wash, samples were incubated with secondary antibodies (594 anti-glucagon
343 and 647 anti-insulin) for 48-72 hr at RT, then washed overnight in TBST. Whole pancreata were
344 then mounted in low melting temp agarose for imaging. Whole pancreata were imaged using a

345 custom light sheet microscope. 2D images were collected in a 3 mm x 5 mm field of view every
346 10 um over a 5 mm volume to generate the 3D reconstruction. Imaris was used to assign
347 surface volumes to pancreas morphology, insulin surfaces, and glucagon surfaces by intensity
348 thresholding.

349

350 **Time Course Image Analysis**

351 All images were analyzed using previously published methods⁴⁵ with custom Matlab
352 (Mathworks) scripts. For activity analysis, images were smoothed using a 5x5 pixel averaging
353 filter. Areas without significant fluorescence were removed. Saturated areas were also removed
354 by limiting the area to intensity below the maximum value. Photobleaching was adjusted for by
355 removing any linear trend. Any islets with significant motion artifacts were removed or time
356 courses were shortened to the time over which no significant movement occurred
357 (displacement of <0.5 cell width). For the time course of each pixel in the image with significant
358 fluorescence, a peak detection algorithm was used to determine if the areas had peak
359 amplitudes significantly above background. A region was considered “active” if the
360 corresponding time course for each pixel had a peak amplitude >2.4x background. The fraction
361 of active area was calculated as the number of pixels detected as “active” across all z-planes,
362 normalized to the total number of pixels that showed significant fluorescence across all z-
363 planes that were not saturated. Islets with significant background fluorescence from spectral
364 overlap of channels were excluded from activity analysis because “inactive” cells were
365 indistinguishable from background and therefore total islet area could not be accurately
366 calculated. Coordination was determined based on coincident timing of identified peaks, where

367 areas were segmented by identified peaks occurring at similar time points. The cross
368 correlation of the time courses for two 5x5 pixel subregion was taken. If the correlation
369 coefficient was >0.75, then the two subregions were considered highly coordinated and merged
370 into a larger region. The coordinated area was calculated as the number of pixels in the largest
371 area of coordination across all z-planes normalized to the total number of pixels of the islet that
372 were determined to be 'active' for all planes. This analysis is based on previous analysis⁴⁵, but
373 adjusted for 3-dimensional data. Phase lag and wave propagation speed was determined as
374 in¹⁰, where 2 regions were chosen manually within a coordinated area within the same z-plane.
375 The phase lag of these regions was calculated from a Fourier transform of each time course.
376 First the peak frequency was identified from the power spectrum, as generated from a Fourier
377 transform of each time course. At each peak frequency the phase was then calculated. The
378 phase lag was calculated from the difference in phase between each region, and converted into
379 a time lag according to $(dt=(1/f)*\tan^{-1}(\varphi_1-\varphi_2))$, where $\varphi_1-\varphi_2$ is the phase difference, and f is
380 the sampling frequency of the time courses analyzed. Speed was calculated by dividing the
381 distance between the two regions by the time lag. For phase and speed analysis only islets with
382 >90% coordinated area was used. All statistical analysis was performed in Prism (Graphpad) or
383 Matlab. First a F-test was used to determine if variances were equal then a Student's t-test or
384 Welch t-test (for unequal variance) were utilized for determining whether activity,
385 coordination, phase lag and speed were significantly different. $p<0.05$ was considered
386 significant.

387 **Figure Legends**

388 **Figure 1: *Robo* β KO islets have fewer homotypic nearest neighbors than controls (A)**

389 Immunofluorescence images (left and middle panels) and cell connectivity maps generated by
390 nearest neighbor analysis (right panels) of control and *Robo* β KO islets. β cells (red), α cells
391 (green), and δ cells (blue) are denoted by nodes on the connectivity maps. A line the same color
392 as both nodes it connects denotes a homotypic interaction of that corresponding cell type. A
393 white line connecting two nodes denotes a heterotypic interaction between cell types. (B)
394 Probability of any homotypic cell-cell contact in *Robo* β KO islets vs controls ($n=9-11$ islets for 3
395 mice from each genotype; control 83.7%, *Robo* β KO 64.43%, p 0.0008). (C) Probability of β cell-
396 β cell contacts in *Robo* β KO islets vs. controls ($n=9-11$ islets for 3 mice from each genotype;
397 control 75.35%, *Robo* β KO 50.37%, $p=0.01$). (D) Probability of any heterotypic cell-cell contact in
398 *Robo* β KO islets vs. controls ($n= 9-11$ islets for 3 mice from each genotype; control 16.3%, *Robo*
399 β KO 35.57%, $p=0.0008$ (E). Probability of β cell- α cell contacts in *Robo* β KO islets vs controls
400 ($n=9-11$ islets for 3 mice from each genotype; control 11.21%, *Robo* β KO 25.99%, $p=0.02$). (B-E
401 Similar shaded points in graphs indicate islets from the same mouse).

402

403 **Figure 2: Control islets show highly synchronized whole islet Ca^{2+} oscillations (A) High**

404 resolution maximum intensity projection of a control islet *in vivo* in an *AAV8-RIP-GCaMP6s*-
405 injected mouse showing GCaMP6s in green, nuclear mCherry β cell lineage-tracing in red, and
406 collagen (second-harmonic fluorescence) in blue. (B) Stills over one oscillation period from
407 control islet in supplementary video 1, starting after blood glucose level reached ~ 300 mg/dL
408 from IP glucose injection. Video was recorded for 10 minutes with frames taken every 10

409 seconds. (C) Representative time courses of Ca^{2+} activity in 4 individual areas from control islet
410 in supplementary video 1 showing correlation over 98% of the active islet area. Time courses
411 are normalized to average fluorescence of individual area over time. Similar color indicates that
412 the time courses have a Pearson's correlation coefficient of ≥ 0.75 and matches the region of
413 coordination that is seen in D. (D) False color map of top five largest coordinated areas across z-
414 stack of control islet from analysis in C. Areas in grey are not coordinated. The color represents
415 a region of coordination with Pearson's Correlation Coefficient ≥ 0.75 of GCaMP6s activity. Cells
416 used in time courses in C are labeled.

417

418 **Figure 3: *Robo* β KO islets show uncoordinated whole islet Ca^{2+} oscillations** (A) High resolution
419 maximum intensity projection of a *Robo* β KO islet *in vivo* in an AAV8-RIP-GCaMP6s-injected
420 mouse showing GCaMP6s in green, nuclear mCherry β cell lineage tracing in red, and collagen in
421 blue. (B) Stills over one oscillation period from *Robo* β KO islet in supplementary video 2,
422 starting after blood glucose level reached ~ 300 mg/dL from IP glucose injection. Video was
423 recorded for 10 minutes with frames taken every 30 seconds. (C) Representative time courses
424 of Ca^{2+} activity in 4 individual areas from *Robo* β KO islet in supplementary video 2, showing
425 correlation of 43.6% of the active islet area. Time courses are normalized to average
426 fluorescence of individual area over time. Similar color indicates that the time courses have a
427 Pearson's correlation coefficient of ≥ 0.75 and matches the region of coordination that is seen in
428 D. (D) False color map of top five largest coordinated areas across z-stack of *Robo* β KO islet
429 from analysis in C. Areas in grey are not coordinated. The color represents a region of

430 coordination with Pearson's Correlation Coefficient ≥ 0.75 of GCaMP6s activity. Cells used in
431 time courses in C are labeled.

432

433 **Figure 4: Quantification of *Robo* β KO Ca^{2+} oscillation phenotype** (A) Largest fraction of area in
434 islet exhibiting coordinated Ca^{2+} oscillations for control and *Robo* β KO islets. (B) Fraction of
435 active islet area showing elevated Ca^{2+} activity for control and *Robo* β KO islets. (C) Phase lag of
436 islet from control and *Robo* β KO islets. Only islets with large coordination across islet ($>90\%$
437 coordinated area) were used. (D) Speed across islets from control and *Robo* β KO islets. Only
438 islets with large coordination across islet ($>90\%$ coordinated area) were used. (E) Close up of
439 time-courses from islet in Figure 2, showing representative phase lag of Ca^{2+} waves of 2 cells in
440 the same z-plane. (F) Same as C but for Supplemental Figure 3.

441

442 **Figure 5: *Robo* β KO islets show heterogeneity in severity of architectural disruption** (A) Space
443 filling models generated from cleared 3x5mm sections of pancreatic tissue from control and
444 *Robo* β KO mice with insulin in red, glucagon in green, and auto-fluorescent surrounding tissue
445 in blue. Projections show surface views of islets with insulin channel shown as transparent in
446 order to visualize α cells on the adjacent side and the interior of the islet. (B) Close ups from
447 portions of the pancreatic tissue showing heterogeneity in architectural phenotype in *Robo* β KO
448 and number of α cells present in both control and *Robo* β KO.

449

450 **Figure 6: Amount of Cx36 gap junctions remains unchanged in *Robo* β KO** (A)
451 Immunofluorescent images showing Cx36 (gray or green) and insulin (red) in *Robo* β KO and

452 control islets. (B) Quantification of area of Cx36 staining normalized to islet area in *Robo* β *KO*
453 islets and controls showing no significant difference ($n=10-12$ islets for 4 mice per group,
454 $p=0.17$).

455

456 **Figure 7: Amount of vascularization remains unchanged in *Robo* β *KO* islets** (A) Representative
457 immunofluorescent staining of basement membrane marking vasculature (laminin and collagen
458 IV) showing similar amounts in *Robo* β *KO* and control islets (B) Quantification of area of staining
459 normalized to islet area showing no difference in amounts of basement membrane marking
460 blood vessels in *Robo* β *KO* compared to control islets.

461 **Supplemental Figures**

462 **Supplemental Video 1: Control islets show highly synchronized Ca^{2+} oscillations.** Intravital time
463 course video of an islet within the *in vivo* pancreas of a control β cell lineage traced mouse
464 infected with *AAV8-Ins1-GCaMP6s*. Lineage traced β cells are marked by mCherry in red and
465 GCaMP6s is shown in green. Mouse was injected IP with glucose, and video was recorded once
466 blood glucose levels reached ~ 300 mg/dL. Images were taken every 10 seconds through a Z-
467 stack of 8 slices each $8\mu\text{m}$ apart, over 10 minutes. Scale bar is $100\mu\text{m}$. Time stamp shown in in
468 upper left corner shows time of image in min:sec.

469

470 **Supplemental Video 2: *Robo* βKO islets show unsynchronized Ca^{2+} oscillations.** Intravital time
471 course video of an islet within the *in vivo* pancreas of a *Robo* βKO β cell lineage traced mouse
472 infected with *AAV8-Ins1-GCaMP6s*, and retro-orbitally injected with rhodamine-dextran to
473 mark vasculature. Lineage traced β cells are marked by mCherry in red and GCaMP6s is shown
474 in green, and vasculature is shown in yellow. Mouse was injected IP with glucose, and video
475 was recorded once blood glucose levels reached ~ 300 mg/dL. Images were taken every 30
476 seconds through a Z-stack of 12 slices each $8\mu\text{m}$ apart, over 10 minutes. Scale bar is $100\mu\text{m}$.
477 Time stamp shown in in upper left corner shows time of image in min:sec.

478

479 **Supplemental Video 3: Most *Robo* βKO islets show unsynchronized Ca^{2+} oscillations.** Intravital
480 time course video of an islet within the *in vivo* pancreas of a *Robo* βKO β cell lineage traced
481 mouse infected with *AAV8-Ins1-GCaMP6s*. Lineage traced β cells are marked by mCherry in red
482 and GCaMP6s is shown in green. Mouse was injected IP with glucose, and video was recorded

483 once blood glucose levels reached ~300 mg/dL. Images were taken every 10 seconds through a
484 Z-stack of 8 slices each 8 μ m apart, over 10 minutes. Scale bar is 100 μ m. Time stamp shown in in
485 upper left corner shows time of image in min:sec.

486

487 **Supplemental Video 4: A subset of *Robo* β KO islets retain synchronized Ca^{2+} oscillations.**

488 Intravital time course video of an islet within the *in vivo* pancreas of a *Robo* β KO β cell lineage
489 traced mouse infected with AAV8-Ins1-GCaMP6s. Lineage traced β cells are marked by mCherry
490 in red and GCaMP6s is shown in green. Mouse was injected IP with glucose, and video was
491 recorded once blood glucose levels reached ~300 mg/dL. Images were taken every 10 seconds
492 through a Z-stack of 8 slices each 8 μ m apart, over 10 minutes. Scale bar is 100 μ m. Time stamp
493 shown in in upper left corner shows time of image in min:sec.

494

495 **Supplemental Figure 1: *Robo* β KO islets retain β cell differentiation and maturity markers**

496 Volcano plot of differential gene expression from bulk RNA sequencing on lineage traced FACS
497 sorted β cells from *Robo* β KO and control mice showing no significant differential gene
498 expression of markers ($n=2$ mice from each group).

499

500 **Supplemental Figure 2: *Robo* β KO islets show uncoordinated whole islet Ca^{2+} oscillations (A)**

501 High resolution maximum intensity projection of a *Robo* β KO islet *in vivo* in an AAV8-RIP-
502 GCaMP6s-injected mouse showing GCaMP6s in green, nuclear mCherry β cell lineage-tracing in
503 red, and collagen (second-harmonic fluorescence) in blue. (B) Stills over one oscillation period
504 from *Robo* β KO islet in supplemental video 2, starting after blood glucose level reached ~300

505 mg/dL from IP glucose injection. Video was recorded for 10 minutes with frames taken every 10
506 seconds. (C) Representative time courses of Ca^{2+} activity in 4 individual areas from *Robo* β KO
507 islet in supplementary video 3, showing correlation of 50% of the active islet area. Time courses
508 are normalized to average fluorescence of individual area over time. Similar color indicates that
509 the time courses have a Pearson's correlation coefficient of ≥ 0.75 and matches the region of coordination that is seen in D. (D) False color
510 map of top five largest coordinated areas across z-stack of *Robo* β KO islet from analysis in C.
511 Areas in grey are not coordinated. The color represents a region of coordination with Pearson's
512 correlation coefficient of ≥ 0.75 of GCaMP6s activity.

514

515 **Supplemental Figure 3: A subset of *Robo* β KO islets show coordinated whole islet Ca^{2+}**
516 **oscillations** (A) High resolution maximum intensity projection of a *Robo* β KO islet *in vivo* in an
517 *AAV8-RIP-GCaMP6s*-injected mouse showing GCaMP6s in green, nuclear mCherry β cell lineage
518 tracing in red, and collagen in blue. (B) Stills over one oscillation period from *Robo* β KO islet in
519 supplementary video 4, starting after blood glucose level reached ~ 300 mg/dL from IP glucose
520 injection. Video was recorded for 10 minutes with frames taken every 10 seconds. (C)
521 Representative time courses of Ca^{2+} activity in 4 individual areas from *Robo* β KO islet in
522 supplementary video 4, showing correlation of 98% of the active islet area. Time courses are
523 normalized to average fluorescence of individual area over time. Similar color indicates that the
524 time courses have a Pearson's correlation coefficient of ≥ 0.75 and matches the region of
525 coordination that is seen in D. (D) False color map of top five largest coordinated areas across z-
526 stack of *Robo* β KO islet from analysis in C. Areas in grey are not coordinated. The color

527 represents a region of coordination with Pearson's correlation coefficient of ≥ 0.75 of GCaMP6s
528 activity.

529

530 References

- 531 1 Kim, A. *et al.* Islet architecture: A comparative study. *Islets* **1**, 129-136,
532 doi:10.4161/isl.1.2.9480 (2009).
- 533 2 Bonner-Weir, S., Sullivan, B. A. & Weir, G. C. Human Islet Morphology Revisited:
534 Human and Rodent Islets Are Not So Different After All. *The journal of histochemistry*
535 *and cytochemistry : official journal of the Histochemistry Society* **63**, 604-612,
536 doi:10.1369/0022155415570969 (2015).
- 537 3 Hoang, D. T. *et al.* A conserved rule for pancreatic islet organization. *PloS one* **9**,
538 e110384, doi:10.1371/journal.pone.0110384 (2014).
- 539 4 Hraha, T. H., Bernard, A. B., Nguyen, L. M., Anseth, K. S. & Benninger, R. K.
540 Dimensionality and size scaling of coordinated Ca(2+) dynamics in MIN6 beta-cell
541 clusters. *Biophysical journal* **106**, 299-309, doi:10.1016/j.bpj.2013.11.026 (2014).
- 542 5 Nittala, A., Ghosh, S. & Wang, X. Investigating the role of islet cytoarchitecture in its
543 oscillation using a new beta-cell cluster model. *PloS one* **2**, e983,
544 doi:10.1371/journal.pone.0000983 (2007).
- 545 6 Ammala, C. *et al.* Exocytosis elicited by action potentials and voltage-clamp calcium
546 currents in individual mouse pancreatic B-cells. *The Journal of physiology* **472**, 665-688,
547 doi:10.1113/jphysiol.1993.sp019966 (1993).
- 548 7 Ashcroft, F. M. & Rorsman, P. K(ATP) channels and islet hormone secretion: new
549 insights and controversies. *Nature reviews. Endocrinology* **9**, 660-669,
550 doi:10.1038/nrendo.2013.166 (2013).
- 551 8 Bertram, R., Sherman, A. & Satin, L. S. Electrical bursting, calcium oscillations, and
552 synchronization of pancreatic islets. *Advances in experimental medicine and biology* **654**,
553 261-279, doi:10.1007/978-90-481-3271-3_12 (2010).
- 554 9 Bertram, R., Satin, L. S. & Sherman, A. S. Closing in on the Mechanisms of Pulsatile
555 Insulin Secretion. *Diabetes* **67**, 351-359, doi:10.2337/dbi17-0004 (2018).
- 556 10 Benninger, R. K., Zhang, M., Head, W. S., Satin, L. S. & Piston, D. W. Gap junction
557 coupling and calcium waves in the pancreatic islet. *Biophysical journal* **95**, 5048-5061,
558 doi:10.1529/biophysj.108.140863 (2008).
- 559 11 Head, W. S. *et al.* Connexin-36 gap junctions regulate in vivo first- and second-phase
560 insulin secretion dynamics and glucose tolerance in the conscious mouse. *Diabetes* **61**,
561 1700-1707, doi:10.2337/db11-1312 (2012).
- 562 12 Brereton, M. F., Vergari, E., Zhang, Q. & Clark, A. Alpha-, Delta- and PP-cells: Are
563 They the Architectural Cornerstones of Islet Structure and Co-ordination? *The journal of*
564 *histochemistry and cytochemistry : official journal of the Histochemistry Society* **63**, 575-
565 591, doi:10.1369/0022155415583535 (2015).
- 566 13 Hang, Y. *et al.* The MafA transcription factor becomes essential to islet beta-cells soon
567 after birth. *Diabetes* **63**, 1994-2005, doi:10.2337/db13-1001 (2014).

- 568 14 Yamagata, K. *et al.* Overexpression of dominant-negative mutant hepatocyte nuclear
569 factor-1 alpha in pancreatic beta-cells causes abnormal islet architecture with decreased
570 expression of E-cadherin, reduced beta-cell proliferation, and diabetes. *Diabetes* **51**, 114-
571 123 (2002).
- 572 15 Gannon, M. *et al.* Persistent expression of HNF6 in islet endocrine cells causes disrupted
573 islet architecture and loss of beta cell function. *Development* **127**, 2883-2895 (2000).
- 574 16 Gu, C. *et al.* Pancreatic beta cells require NeuroD to achieve and maintain functional
575 maturity. *Cell metabolism* **11**, 298-310, doi:10.1016/j.cmet.2010.03.006 (2010).
- 576 17 Ahlgren, U., Jonsson, J., Jonsson, L., Simu, K. & Edlund, H. beta-cell-specific
577 inactivation of the mouse *Ipf1/Pdx1* gene results in loss of the beta-cell phenotype and
578 maturity onset diabetes. *Genes & development* **12**, 1763-1768 (1998).
- 579 18 Borden, P., Houtz, J., Leach, S. D. & Kuruvilla, R. Sympathetic innervation during
580 development is necessary for pancreatic islet architecture and functional maturation. *Cell*
581 *reports* **4**, 287-301, doi:10.1016/j.celrep.2013.06.019 (2013).
- 582 19 Doyle, M. J. & Sussel, L. *Nkx2.2* regulates beta-cell function in the mature islet.
583 *Diabetes* **56**, 1999-2007, doi:10.2337/db06-1766 (2007).
- 584 20 Sinagoga, K. L. *et al.* Distinct roles for the mTOR pathway in postnatal morphogenesis,
585 maturation and function of pancreatic islets. *Development* **144**, 2402-2414,
586 doi:10.1242/dev.146316 (2017).
- 587 21 Huang, C. *et al.* Synaptotagmin 4 Regulates Pancreatic beta Cell Maturation by
588 Modulating the Ca(2+) Sensitivity of Insulin Secretion Vesicles. *Developmental cell* **45**,
589 347-361 e345, doi:10.1016/j.devcel.2018.03.013 (2018).
- 590 22 Jimenez-Caliani, A. J. *et al.* alphaE-Catenin Is a Positive Regulator of Pancreatic Islet
591 Cell Lineage Differentiation. *Cell reports* **20**, 1295-1306,
592 doi:10.1016/j.celrep.2017.07.035 (2017).
- 593 23 Bastidas-Ponce, A. *et al.* *Foxa2* and *Pdx1* cooperatively regulate postnatal maturation of
594 pancreatic beta-cells. *Molecular metabolism* **6**, 524-534,
595 doi:10.1016/j.molmet.2017.03.007 (2017).
- 596 24 Crawford, L. A. *et al.* Connective tissue growth factor (CTGF) inactivation leads to
597 defects in islet cell lineage allocation and beta-cell proliferation during embryogenesis.
598 *Mol Endocrinol* **23**, 324-336, doi:10.1210/me.2008-0045 (2009).
- 599 25 Szabat, M. *et al.* Reduced Insulin Production Relieves Endoplasmic Reticulum Stress and
600 Induces beta Cell Proliferation. *Cell metabolism* **23**, 179-193,
601 doi:10.1016/j.cmet.2015.10.016 (2016).
- 602 26 Brissova, M. *et al.* Islet microenvironment, modulated by vascular endothelial growth
603 factor-A signaling, promotes beta cell regeneration. *Cell metabolism* **19**, 498-511,
604 doi:10.1016/j.cmet.2014.02.001 (2014).
- 605 27 Baetens, D. *et al.* Alteration of islet cell populations in spontaneously diabetic mice.
606 *Diabetes* **27**, 1-7 (1978).
- 607 28 Starich, G. H., Zafirova, M., Jablenska, R., Petkov, P. & Lardinois, C. K. A
608 morphological and immunohistochemical investigation of endocrine pancreata from
609 obese *ob+/ob+* mice. *Acta histochemica* **90**, 93-101, doi:10.1016/S0065-1281(11)80167-
610 4 (1991).
- 611 29 Kilimnik, G. *et al.* Altered islet composition and disproportionate loss of large islets in
612 patients with type 2 diabetes. *PloS one* **6**, e27445, doi:10.1371/journal.pone.0027445
613 (2011).

- 614 30 Nir, T., Melton, D. A. & Dor, Y. Recovery from diabetes in mice by beta cell
615 regeneration. *The Journal of clinical investigation* **117**, 2553-2561,
616 doi:10.1172/JCI32959 (2007).
- 617 31 Adams, M. T., Gilbert, J. M., Hinojosa Paiz, J., Bowman, F. M. & Blum, B. Endocrine
618 cell type sorting and mature architecture in the islets of Langerhans require expression of
619 Roundabout receptors in beta cells. *Scientific reports* **8**, 10876, doi:10.1038/s41598-018-
620 29118-x (2018).
- 621 32 Hoang, D. T., Hara, M. & Jo, J. Design Principles of Pancreatic Islets: Glucose-
622 Dependent Coordination of Hormone Pulses. *PloS one* **11**, e0152446,
623 doi:10.1371/journal.pone.0152446 (2016).
- 624 33 Reissaus, C. A. *et al.* A Versatile, Portable Intravital Microscopy Platform for Studying
625 Beta-cell Biology In Vivo. *Scientific reports* **9**, 8449, doi:10.1038/s41598-019-44777-0
626 (2019).
- 627 34 Ravier, M. A. *et al.* Loss of connexin36 channels alters beta-cell coupling, islet
628 synchronization of glucose-induced Ca²⁺ and insulin oscillations, and basal insulin
629 release. *Diabetes* **54**, 1798-1807 (2005).
- 630 35 Yang, Y. H., Manning Fox, J. E., Zhang, K. L., MacDonald, P. E. & Johnson, J. D.
631 Intra-islet SLIT-ROBO signaling is required for beta-cell survival and potentiates insulin
632 secretion. *Proceedings of the National Academy of Sciences of the United States of*
633 *America* **110**, 16480-16485, doi:10.1073/pnas.1214312110 (2013).
- 634 36 Blockus, H. & Chedotal, A. Slit-Robo signaling. *Development* **143**, 3037-3044,
635 doi:10.1242/dev.132829 (2016).
- 636 37 Sneddon, J. B. *et al.* Stem Cell Therapies for Treating Diabetes: Progress and Remaining
637 Challenges. *Cell stem cell* **22**, 810-823, doi:10.1016/j.stem.2018.05.016 (2018).
- 638 38 Nasteska, D., Vilorio, K., Everett, L. & Hodson, D. J. Informing beta-cell regeneration
639 strategies using studies of heterogeneity. *Molecular metabolism* **27S**, S49-S59,
640 doi:10.1016/j.molmet.2019.06.004 (2019).
- 641 39 Roscioni, S. S., Migliorini, A., Gegg, M. & Lickert, H. Impact of islet architecture on
642 beta-cell heterogeneity, plasticity and function. *Nature reviews. Endocrinology* **12**, 695-
643 709, doi:10.1038/nrendo.2016.147 (2016).
- 644 40 Branchfield, K. *et al.* Pulmonary neuroendocrine cells function as airway sensors to
645 control lung immune response. *Science* **351**, 707-710, doi:10.1126/science.aad7969
646 (2016).
- 647 41 Thorens, B. *et al.* Ins1(Cre) knock-in mice for beta cell-specific gene recombination.
648 *Diabetologia* **58**, 558-565, doi:10.1007/s00125-014-3468-5 (2015).
- 649 42 van der Meulen, T. *et al.* Virgin Beta Cells Persist throughout Life at a Neogenic Niche
650 within Pancreatic Islets. *Cell metabolism* **25**, 911-926 e916,
651 doi:10.1016/j.cmet.2017.03.017 (2017).
- 652 43 Blum, B. *et al.* Reversal of beta cell de-differentiation by a small molecule inhibitor of
653 the TGFbeta pathway. *eLife* **3**, e02809, doi:10.7554/eLife.02809 (2014).
- 654 44 Tran Thi Nhu, H., Arrojo, E. D. R., Berggren, P. O. & Boudier, T. A novel toolbox to
655 investigate tissue spatial organization applied to the study of the islets of Langerhans.
656 *Scientific reports* **7**, 44261, doi:10.1038/srep44261 (2017).
- 657 45 Westacott, M. J. *et al.* Age-Dependent Decline in the Coordinated [Ca(2+)] and Insulin
658 Secretory Dynamics in Human Pancreatic Islets. *Diabetes* **66**, 2436-2445,
659 doi:10.2337/db17-0137 (2017).

Figure 1

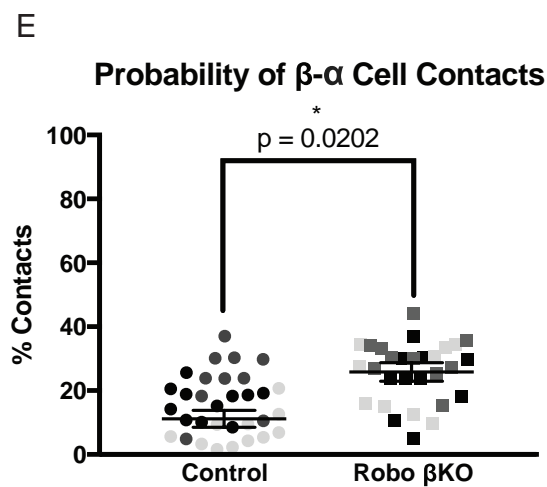
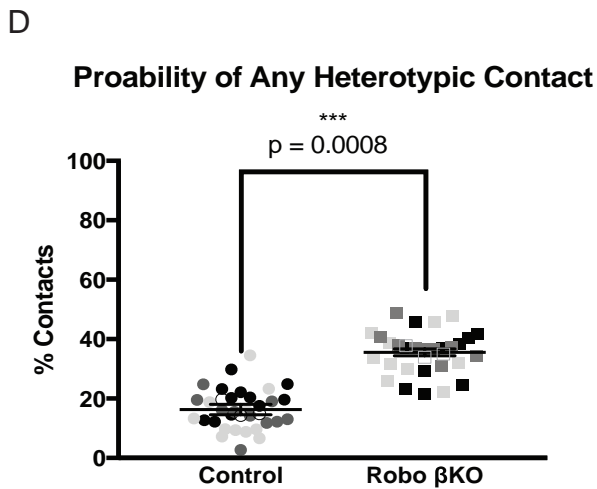
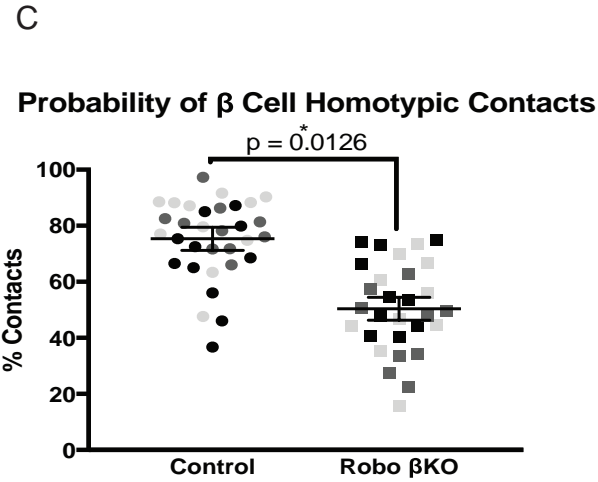
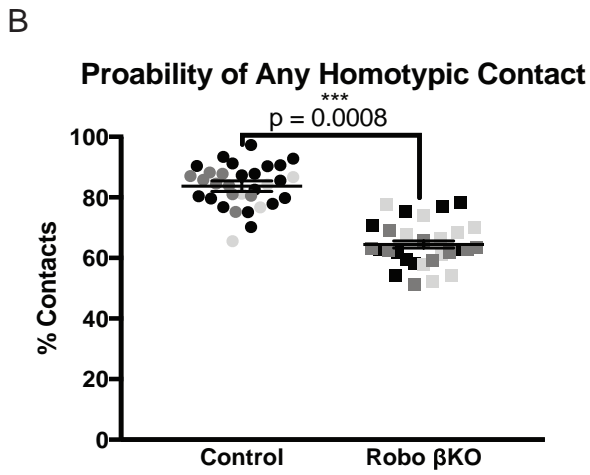
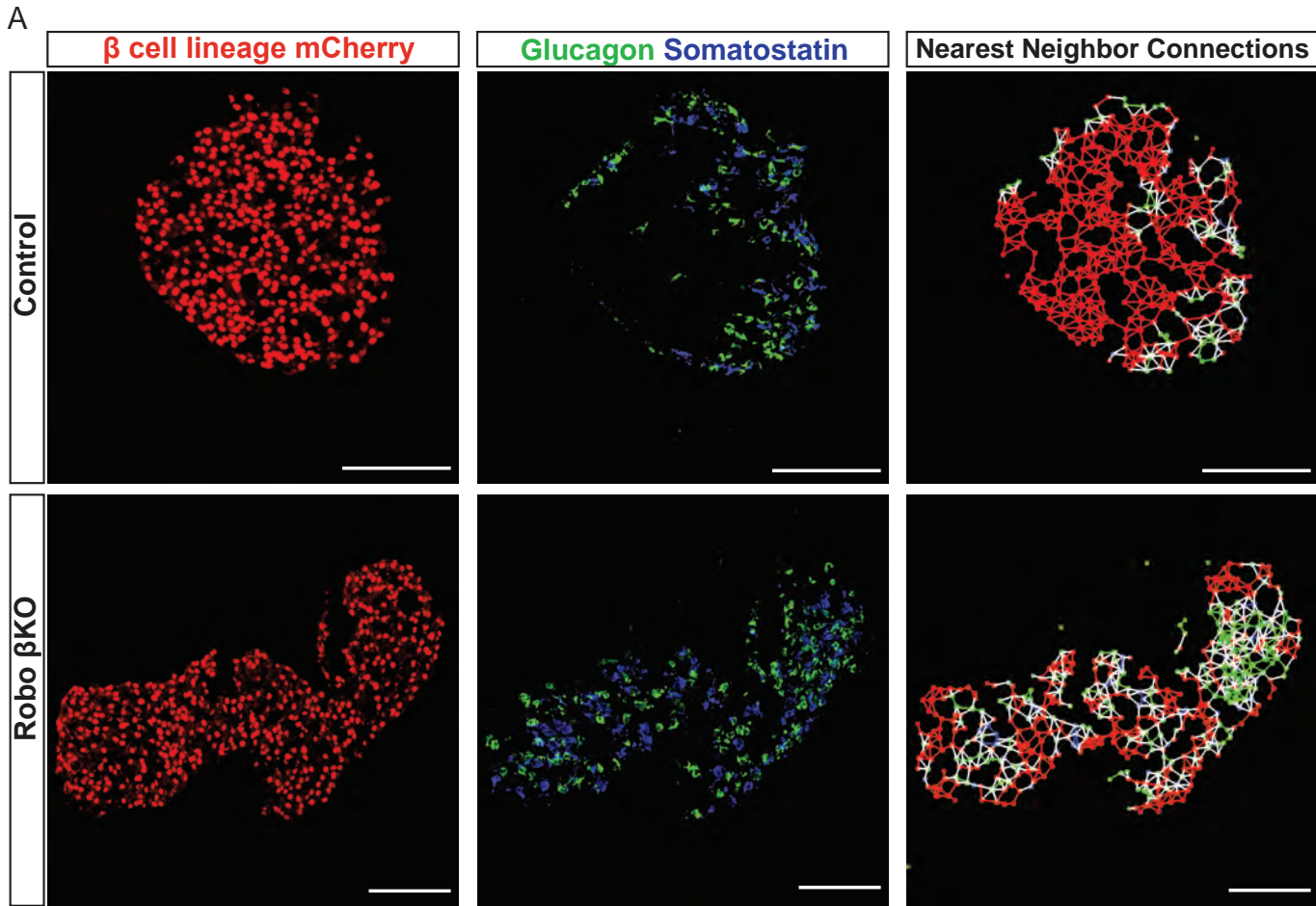
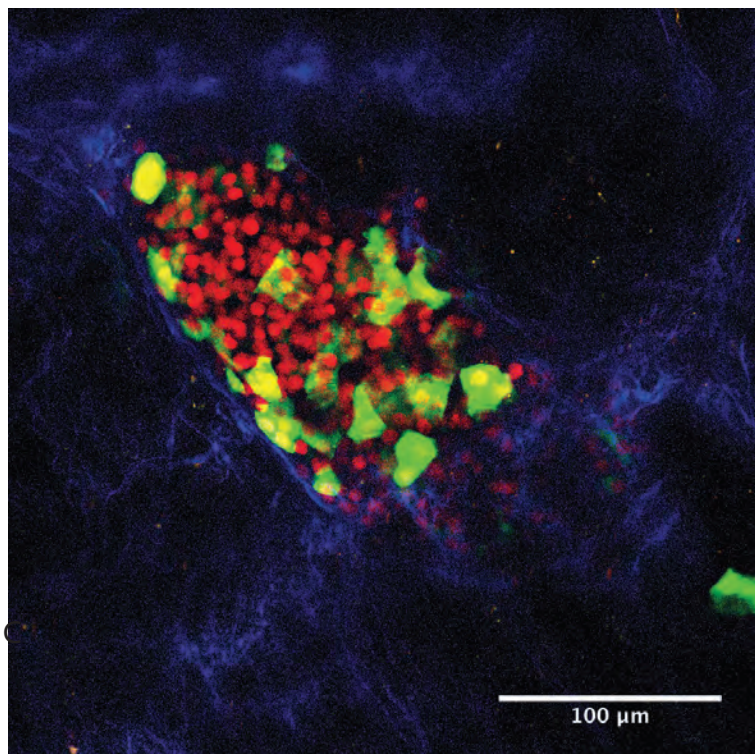
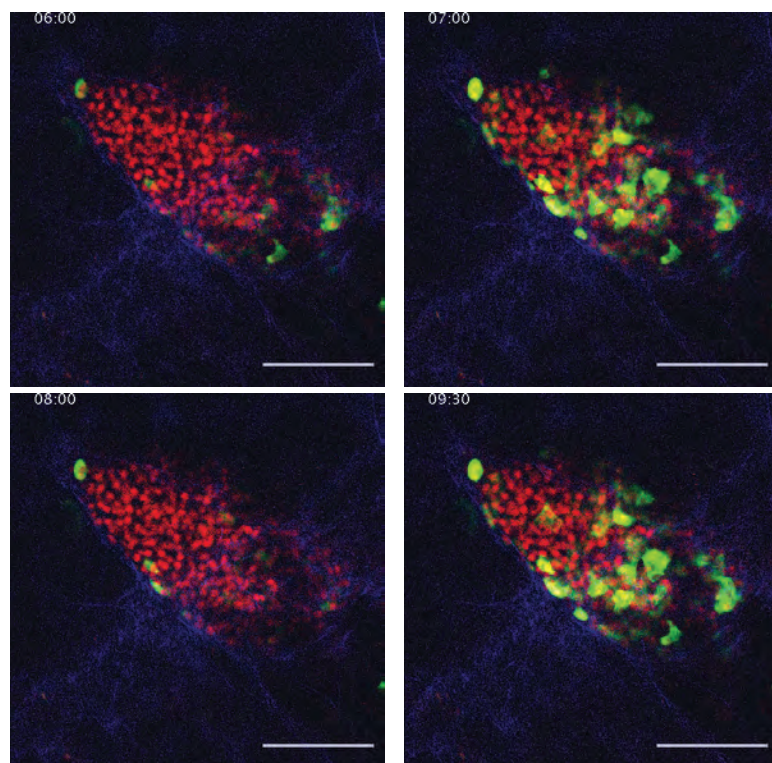


Figure 2

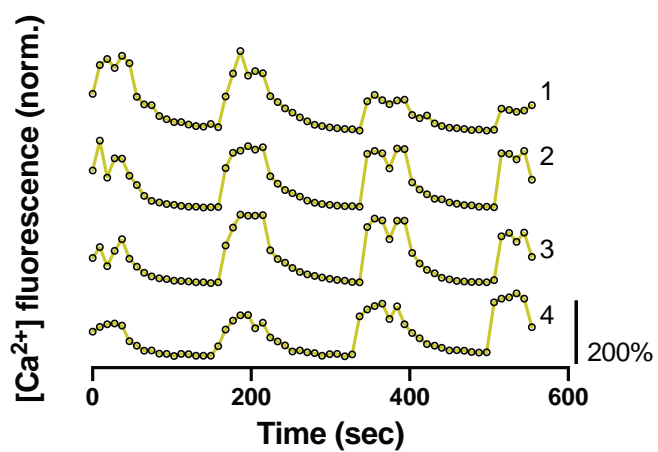
A



B



C



D

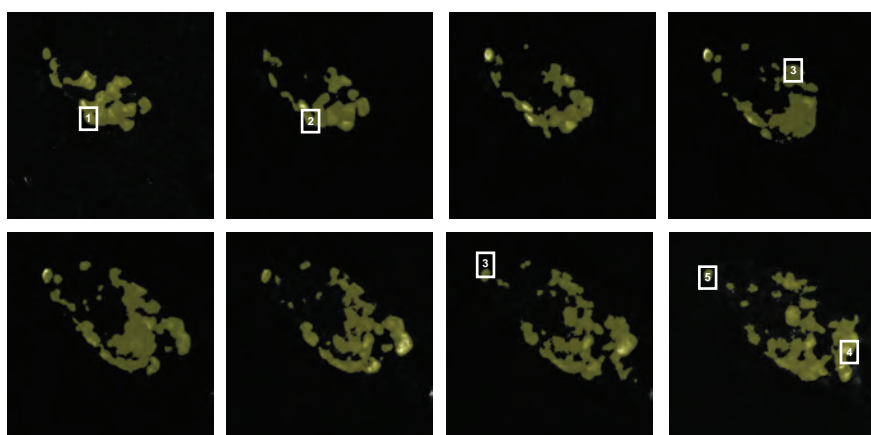
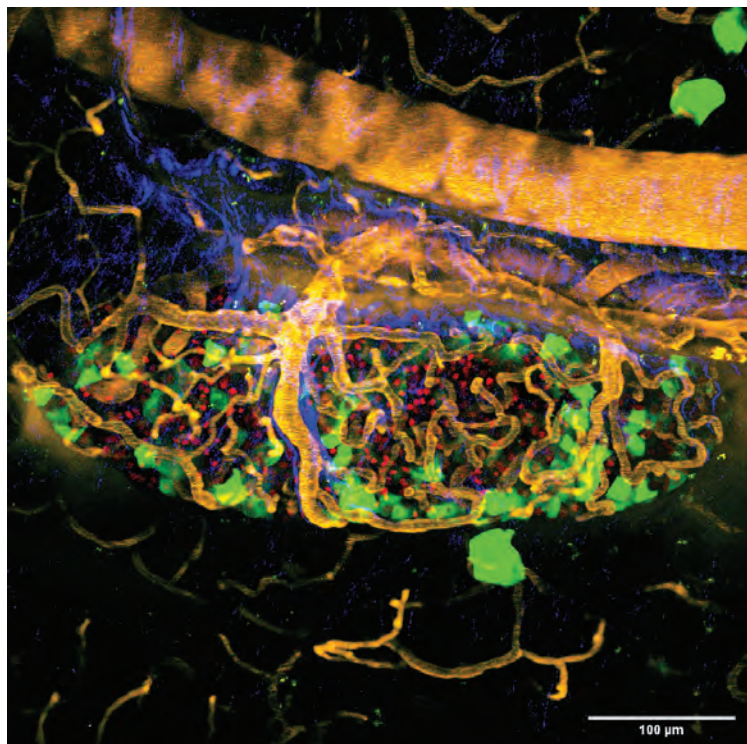
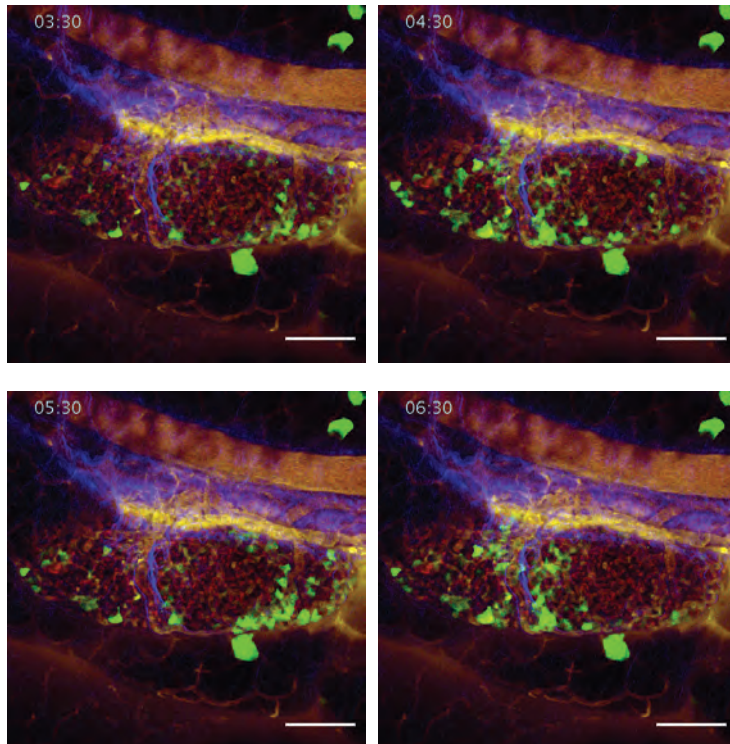


Figure 3

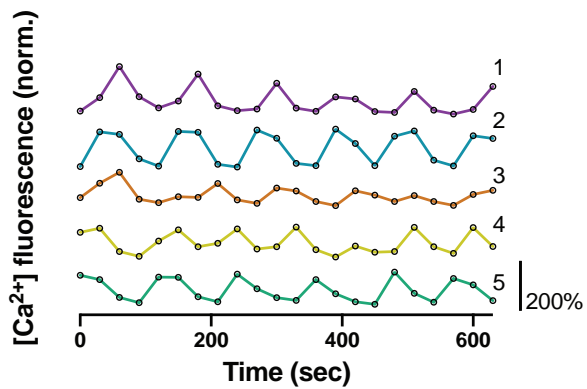
A



B



C



D

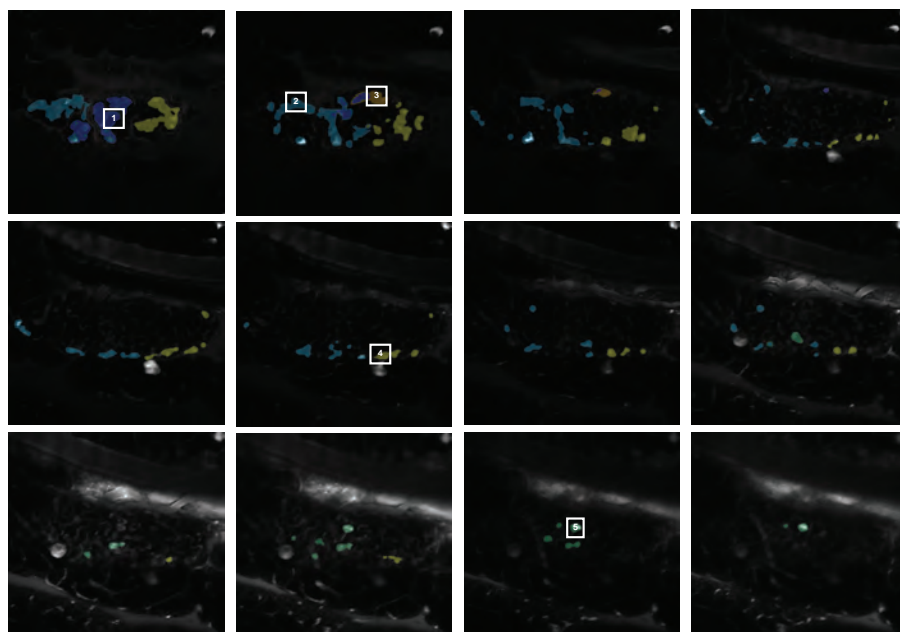


Figure 4

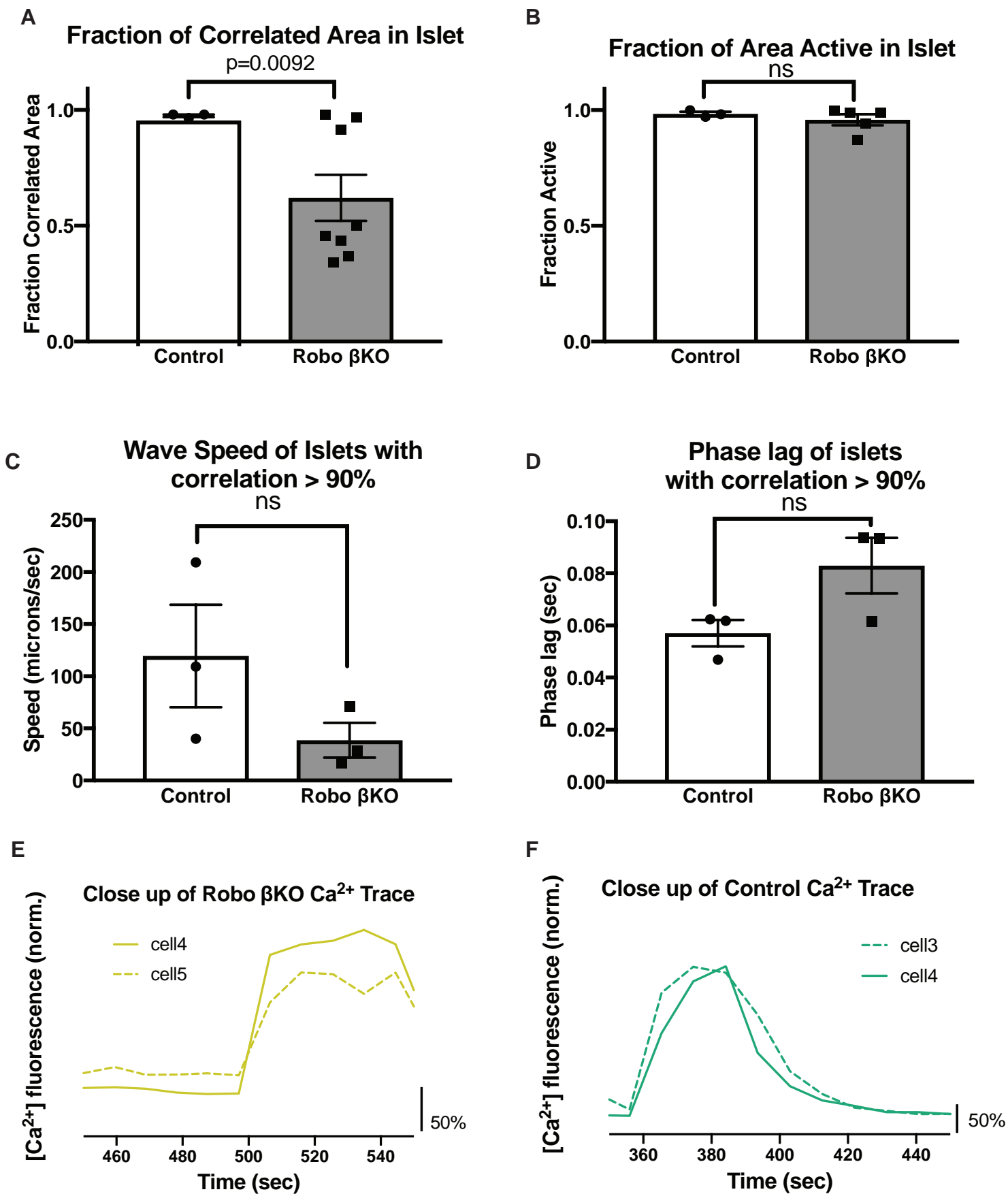


Figure 5

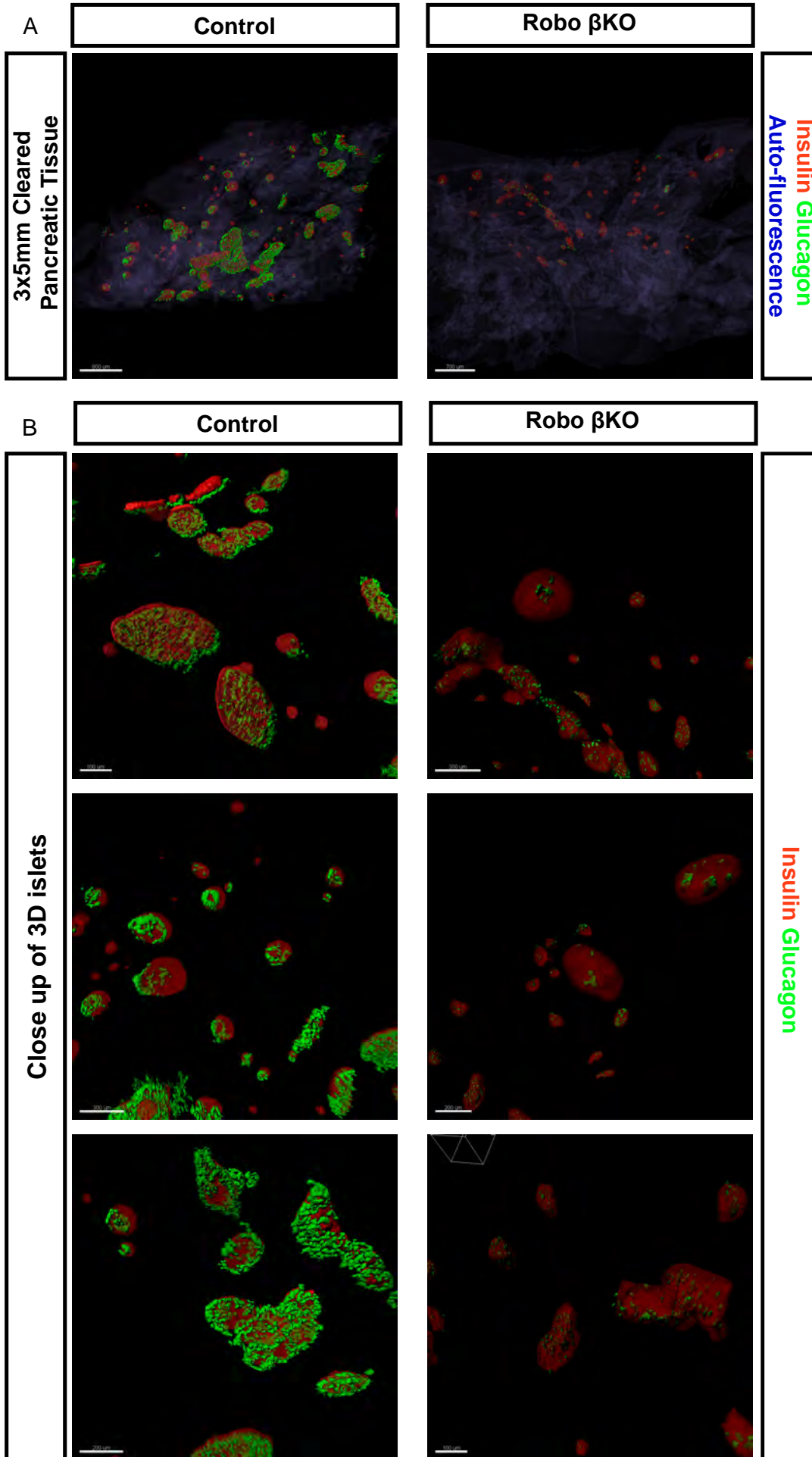
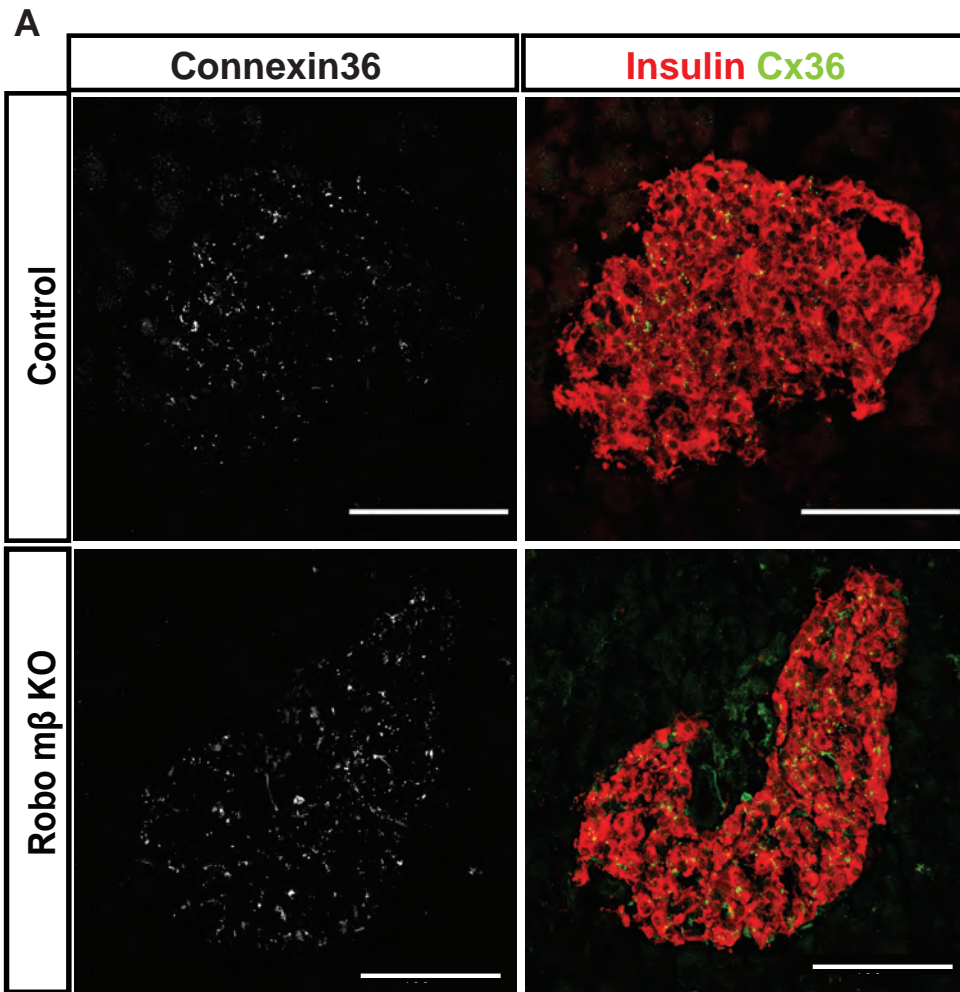


Figure 6



B

Connexin36 in Robo β KO islets vs. Controls

n.s. $p = 0.17$

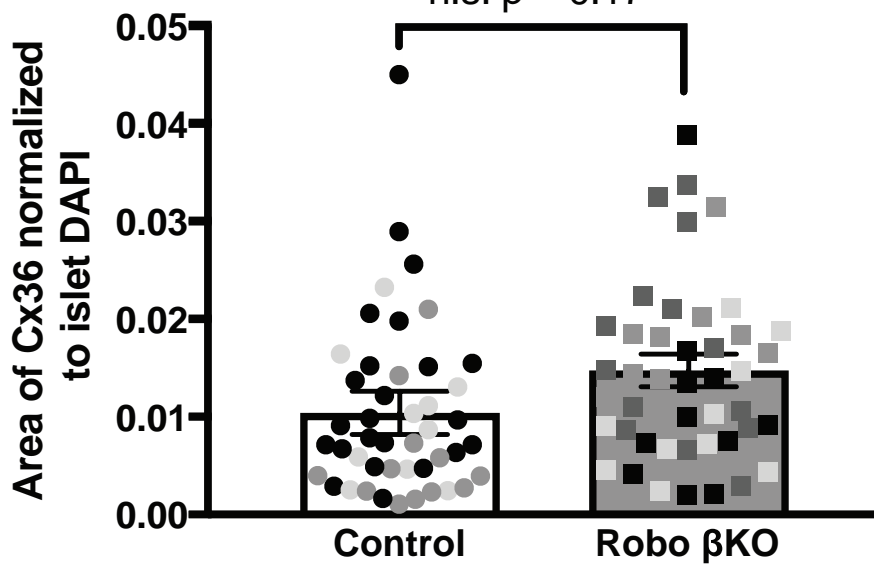


Figure 7

